Solid-catalyzed transport limitations assessment in gas-phase conversion of ethanol to hydrogen over Ni-promoted MMT/TiO2 nano clay catalyst

William Mulewa[1,2*] Titus Tunje Kadere[1]

[1]Department of Engineering and Technology, Technical University of Mombasa, 90420 Mombasa, 80100 Kenya; [2]Chemical and Petroleum Engineering Department, UAE University, 15551 - Al Ain, United Arab Emirates

* Corresponding author's email: wmulewa@tum.ac.ke

Abstract

Mass transport constraints were investigated as they relate to the conversion of ethanol to hydrogen in the gas phase over a Nickel-Montmorillonite/Titanium oxide nanoparticle catalyst. Catalyst synthesis was performed via a modified sol-gel/ impregnation method. Ethanol was dehydrated catalytically using a tube-shaped packed bed reactor while catalyst characterization was through FTIR, XRD, SEM-EDX, TGA, and BET analysis. The Weisz-Prater and Mears' criteria were analyzed theoretically, and the catalyst particle size and reactant flow rate were adjusted experimentally to determine transport limitations. The results demonstrate an absence of gas-phase and intra-particle diffusion limitations for catalyst pellet diameter $\left(d_p \leq 6\ \mu m\right)$. This is attributed to the high effectiveness factor $(\eta > 0.9)$ for particles obtained theoretically. Besides, the high fractional conversion $(X_{ethanol} \cong 0.88)$ obtained experimentally is an indication of constant ethanol conversion because there are no limitations on mass transfer. Ni-promoted MMT/TiO2 nanoparticle catalyst offers great promise for use in ethanol steam reforming for selective and cost-effective hydrogen production, as can be deduced from the results presented here.

Key Words: Hydrogen; Ethanol conversion; Mass transfer limitation; Nanoclay catalyst; Effectiveness factor

Introduction

Energy is deeply ingrained in all three facets of human progress (economic, social, and environmental). More so, the current global energy supply and consumption are prominently reliant on fossil fuel stocks (Hussein, 2023). Hydrogen (H_2) has the potential to reduce reliance on fossil fuels in the long run, since it produces no carbon emissions during its oxidation reactions, which instead yield water vapor (Sahoo et al., 2021). The energy efficiency and environmental impact of H_2 are, however, highly dependent on the methods used to produce it. H_2 may be extracted from a wide range of materials, including renewables like biomass and nonrenewable like natural gas, oil, and coal. Reforming or gasifying natural gas, electrolyzing water, reforming renewable liquids, fermenting sugar-rich feedstocks from biomass, and so on are all viable production options (Megía et al., 2021).The creation of energy-dense H2 from biofuels is a sustainable option that can lessen reliance on finite, regionally restricted, and polluting fossil fuel-based energy sources, according to various studies (Muradov, 2017). Furthermore, viable alternative renewable sources such as wind and solar have demonstrated a fluctuating and intermittent nature, and hence, unreliable (Heard et al., 2017). The most popular method for producing energy from hydrocarbons (HCs), particularly natural gas, is steam reforming (SR). However, the use of fossil fuels as a feedstock and

the resulting CO2 emissions makes SR of HCs unsustainable. Oxygenated HCs such as bio-oil (Pafili et al., 2021), glycerol (Fasolini et al., 2019), methanol (Ranjekar & Yadav, 2021), and ethanol (Liu et al., 2022) have instead been the focus of recent studies.

Ethanol (EtOH) reforming has attracted the most attention because of the abundance of H_2 in the product mixture, has low toxins, and can be more easily separated than the other oxygenated hydrocarbons (Mielenz, 2001). Bioethanol, a renewable kind of ethanol derived from biomass fermentation, is already on the market. Carbon dioxide (CO_2) released during the fermentation process can be reused in the development of biomass, making the manufacture of bio-ethanol a carbon-neutral process (Deluga et al., 2004). Partial oxidative (POX), auto-thermal (ATR), and ethanol steam reforming (ESR) are the three primary methods for reforming EtOH for H_2 generation (Sun et al., 2012). POX is an exothermic chemical reaction as presented by reaction Eq. **Error! Reference source not found.**. Since no external heat input is required, it exhibits faster start-up and response times as compared to ESR. Additionally, due to the lack of water as a reactant, the POX reaction can evaporate the fuel being reformed at a lower temperature than the ATR and ESR reactions (Kraleva et al., 2015). The cost of POX can be further reduced by using air instead of O_2 as an oxidant in the reaction.

$$C_2H_5OH + \frac{3}{2}O_2 \rightarrow 2\,CO_2 + 3\,H_2 \;...\; \Delta H = -554\ kJ/mol \quad \text{..... (1)}$$

Nonetheless, the best that can be achieved in ESR is just half of the predicted theoretical yield of POX reforming (each mole of EtOH reacted produces 3 moles of H_2 gas). Moreover, the stoichiometric proportion of O_2 is crucial to the final POX reforming products. When the amount of O2 is doubled to 3 in reaction Eq. **Error! Reference source not found.**, water is produced instead of H2. Because of this, the POX reforming reaction is highly sensitive and unpredictable (Sawatmongkhon et al., 2019). Combining ESR and POX reforming results in ATR, also known as oxidative steam reforming (OSR). This setup strikes an acceptable balance between hydrogen production and process energy efficiency. When oxygen (O_2) is present in the reaction mixture, carbon species produced in by-products are more easily removed while a feed composition built according to chemical reaction Eq. **Error! Reference source not found.** ensures thermal neutrality (Graschinsky et al., 2012).

$$C_2H_5OH + 1.78\,H_2O + 0.61\,O_2 \rightarrow 2\,CO_2 + 4.78\,H_2 \;...\; \Delta H = 0\ kJ/mol \quad \text{..... (2)}$$

Cost considerations mean that air is typically chosen over O_2 in ATR, just as they are in POX reforming. Regrettably, the inert N_2 in the air slows down the collisions between the reactants and the catalysts. Besides, H_2O presence in the feed stream of ATR also adds to the energy requirement of the system while when compared to ESR, H_2 yield is lower for EtOH ATR.

Ethanol steam reforming (ESR) is an endothermic chemical reaction that, in an ideal case, transforms a gaseous EtOH/H2O mixture into H_2-rich gas and carbon dioxide (CO_2). Since this is an endothermic process, increasing the reaction temperature causes the equilibrium to move to the right and leads to increased conversion of EtOH into H_2 gas. Noteworthy, ethanol and water stoichiometric quantities considerably impact product distribution. The ratio of EtOH to H_2O in the feed is crucial to the yield of H_2 from SR of EtOH. Theoretical H2 production for an EtOH and H2O equimolar feed is 4 mol H2/ mol EtOH. Yet, as shown by reaction Eq. **Error! Reference source not found.**, the theoretical maximum H_2 production from full steam reforming is 6 mole per mole of EtOH.

$$C_2H_5OH + 3\,H_2O \leftrightarrow 6\,H_2 + 3\,CO_2 \;\; ... \;\; \Delta H = 174\ kJ/mol \quad \text{.....(3)}$$

Other side-products such as carbon monoxide (CO) and methane (CH_4) are usually detected depending on feed composition and reaction temperature (Mulewa et al., 2017a). Additionally, although high temperatures are synonymous with high yields of hydrogen, this makes ESR a

slow start-up process that needs external energy input. Due to the advantage in H_2 yield, this study concentrated on ethanol steam reforming.

Heterogeneously, various catalytic compositions have been formulated for ESR. A variety of catalyst supports such as Al_2O_3, ZrO_2, MgO and TiO_2 have been utilized, among which TiO_2 has become most prominent owing to its inexpensive cost, great surface area for metal dispersion, good chemical and mechanical stability, and lack of toxicity. Moreover, Rh, Ru, Pd, Ir, Ni, Co, Cu, and Fe metal-loaded systems have reported higher activity than bare TiO_2 (Hou et al., 2015). More specifically, the high potential for the application of TiO_2 in gas-phase ESR for selective and economical hydrogen production was investigated through a Nickel-promoted Montmorillonite/Titanium oxide (Ni/MMT-TiO_2) nano clay catalyst in a previous study (Mulewa et al., 2017b).

Apart from the catalytic composition, the full utilization of the surface in a heterogeneous catalyzed system is highly dependent on the transport of reacting species within the pore structure of a pellet. In reaction conditions where transport resistances are significant, catalyst performance concerning true activation energies and reaction orders are not observed. Due to species conversion and diffusion as the reaction proceeds, activity on the pellet surface reduces while the concentration of products within the pores increases (Suchorski & Rupprechter, 2018). Interphase/gas-phase diffusion involves the movement of molecules via a fluid layer surrounding the catalyst; intra-particle diffusion involves the movement of molecules through the pore of the catalyst itself within a pellet. Any significant resistance to these two forms of diffusion results in transport limitation and inhibits contact between reactants and the active sites of a catalyst pellet. In theoretical studies, analysis of transport limitations makes use of various dimensionless numbers from the field of transport phenomena (Venerus & Öttinger, 2018). Experimentally, the conversion of reactants is observed while varying both particle size and feed flow rate.

Ethanol was dehydrated to hydrogen gas in a tube-shaped packed bed reactor using a Ni-promoted MMT/TiO_2 nanoparticle (Ni0.12-MMT0.20/TNP) catalyst given that MMT's ability to better distribute Ni on TiO_2 supports has the potential to enhance the interaction between reactant species and catalyst active sites. Modified sol-gel and impregnation techniques were employed in the catalyst synthesis (Shin et al., 2020). Catalyst particles were analyzed using XRD (for crystallographic structure), FTIR spectroscopy (for compound identification), SEM-EDX (for elemental composition), and BET (for pore size distributions and surface area measurements) before and after the reaction. The purpose of this research is to determine the relative importance of intra-particle and gas-phase mass transport limitations through a combination of theoretical and experimental approaches. By analyzing the effects of varying feed flow, pellet diameter, and spacetime, the Thiele modulus, effectiveness, and total effectiveness factors were calculated.

Materials and Methods

Materials and Preparation of the Catalyst

Catalyst synthesis of Ni0.12-MMT0.20/TNPs was carried out using the following chemicals: TTIP [Ti(OCH(CH_3)2)4] as a supply of TiO_2, isopropyl alcohol [(CH3)2CHOH], ethanoic acid [CH_3COOH], Montmorillonite (MMT) [Al2H2Na2O13Si4] and [Ni(NO_3)2·6H_2O] as a supply of Ni. At first, MMT/TiO_2 nanoparticles (MMT/TNPs) were produced using a modified version of the single-step sol-gel synthesis technique. The catalyst synthesis process is presented in **Error! Reference source not found.**. The Titanium solution precursory was created by hydrolyzing isopropanol-based titanium solution with drop-by-drop additions of 1M ethanoic acid diluted in isopropanol at room temperature. Drop by drop, by adding enough MMT dissolved in isopropanol to the titanium sol and continuing to stir the mixture, a thick sol was formed. The slurry was then aged, dried, and calcined. Finally, Ni was impregnated by mixing and stirring a suitable quantity of Ni (NO_3)2·6H_2O combined with MMT/TNPs suspended in deionized water, after which drying, grinding, and calcining were performed. Differently, for microparticles (Ni0.12-MMT0.20/MPs), TiO_2 powder is used instead of titanium isopropoxide (Ti (OCH(CH_3)2)4). The

anatase phase of TiO_2 was obtained by calcining both the micro and nanoparticle samples at 500 °C for 5 hours; this phase is more conducive to the production of H_2 gas (Gullapelli et al., 2017).

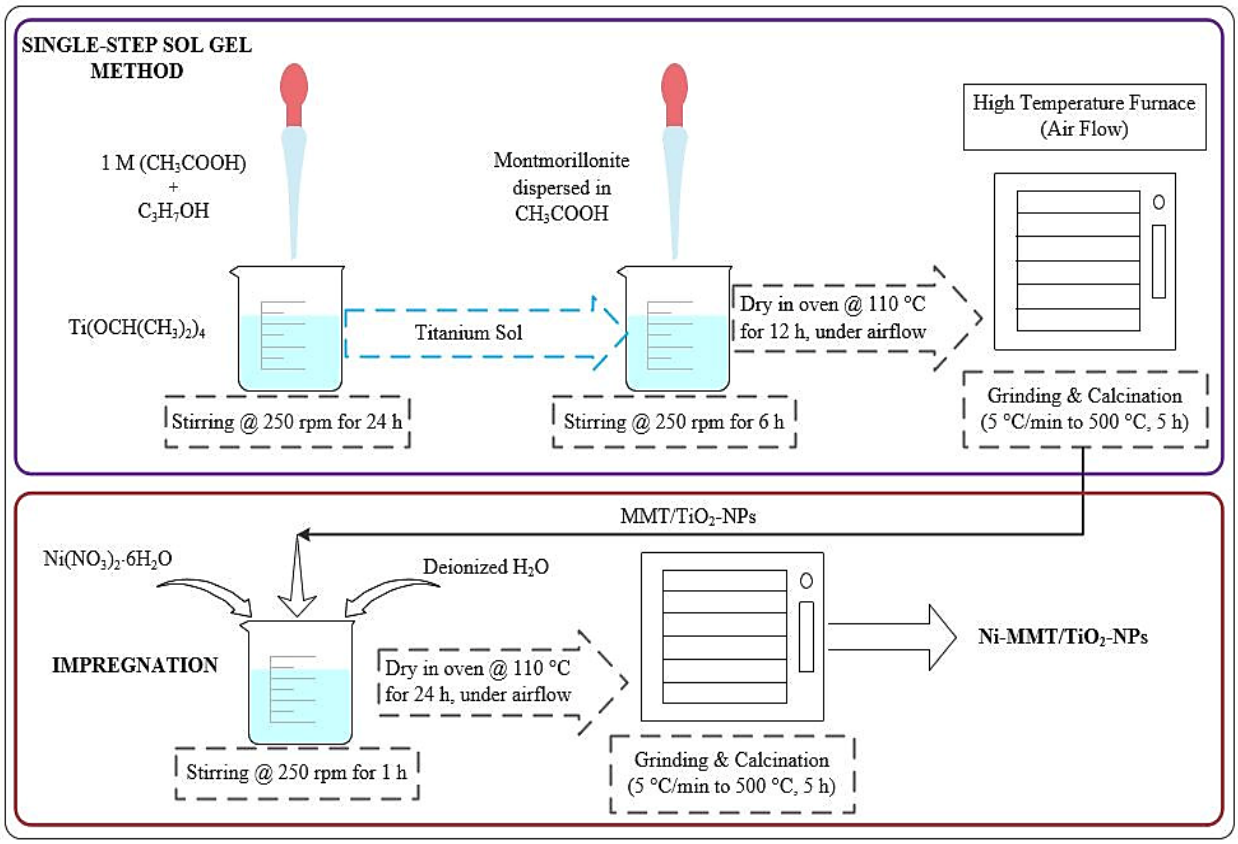

Figure 1. Catalyst synthesis process

Characterization of Catalysts

Crystalline structure and phase transitions in samples were studied by X-ray diffraction (XRD). The microstructure, surface shape, and quantitative elemental analysis of the catalysts were all studied using scanning electron microscopy (SEM) accompanied by an energy-dispersive X-ray (EDX) spectrometer. Furthermore, the catalyst's morphology was studied with a field emission scanning electron microscope (FE-SEM). Thermogravimetric Analysis (TGA) was performed on fresh and spent catalyst particle samples to assess the level of coke deposition that had occurred on the catalysts. Catalyst pellet surface areas and pore size distributions were calculated using the Brunauer-Emmett-Teller (BET) analysis (Tahir et al., 2017).

Experimental

The effectiveness of the Ni0.12-MMT0.20/TNPs as catalysts for the conversion of ethanol to produce H_2 was conducted in a tubular packed bed reactor (TPBR). Ni0.12-MMT0.20/TNPs (0.5 g, with a 1:1 weight dilution in quartz, occupying ~ 1 cm) were placed in the annular section of a borosilicate glass tube (8 mm ID and 29 cm length). A carrier gas (N_2) flowing at 40 mL/h introduced the 2 mL/h gaseous EtOH/H_2O mixture (mole ratio of 1:10) into the reactor. Atmospheric pressure was used throughout the isothermal operation of the reactor at 500 °C. Liquid products were evaluated using an offline Agilent 7820A gas chromatograph (GC) system, whereas gaseous products were studied using an online Agilent 6890N network GC system (Tahir et al., 2017). All reported results were after 8 h reaction time and under steady-state conditions

unless otherwise stated. Ethanol conversion, H_2 yield, and selectivity were computed using Eq. **Error! Reference source not found.**, **Error! Reference source not found.** and **Error! Reference source not found.** (Fogler, 2016). Here, X denotes conversion, F represents the molar flow rate, and Y and S are yield and selectivity, respectively.

$$X_{\text{ethanol}}\ (\%) = \frac{\left(F^{\text{in}}_{\text{ethanol}} - F^{\text{out}}_{\text{ethanol}}\right)}{F^{\text{in}}_{\text{ethanol}}} \times 100 \quad \text{..... (4)}$$

$$Y_{H_2}\ (\%) = \frac{F^{\text{out}}_{H_2}}{6 \times F^{\text{in}}_{\text{ethanol}}} \times 100 \quad \text{..... (5)}$$

$$S_{H_2}\ (\%) = \frac{F^{\text{out}}_{H_2}}{\sum_{\text{j}} F^{\text{out}}_{\text{J}}} \times 100 \quad \text{..... .....(6)}$$

Kinetic Parameters

For simplicity and to keep up with the numerous calculations, the ethanol steam reforming reaction equation was simplified to the form of Eq. **Error! Reference source not found.**:

$$\text{Ethanol (A)} + \text{Water (B)} \rightarrow \text{Hydrogen} + \text{Carbon Dioxide} + \text{Side Products} \quad \text{.....(7)}$$

Given the feed had water in excess, the rate of reaction was determined in terms of ethanol conversion, Eq. **Error! Reference source not found.**:

$$-r_{\text{A}} = \frac{\text{d}X_{\text{A}}}{\text{d}\left(V/F_{\text{A0}}\right)} \quad \text{..... (8)}$$

Furthermore, the feed water ratio (γ) and the expansion factor (ε) for changes between reactant and product volumes were taken into account in determining the total molar flow rate (F_{T}), total molar concentration (C_{T}), the molar fraction of ethanol (y_{A}), and ethanol concentration (C_{A}) as per Eq. **Error! Reference source not found.**, **Error! Reference source not found.**, **Error! Reference source not found.** and **Error! Reference source not found.**, respectively.

$$F_{\text{T}} = F_{\text{A0}}\left(1 + \varepsilon X_{\text{A}} + \gamma\right) \quad \text{.....(9)}$$

$$C_{\text{T}} = C_{\text{A0}}\left(1 + \varepsilon X_{\text{A}} + \gamma\right) \quad \text{.....(10)}$$

$$y_{\text{A}} = \frac{\left(1 - X_{\text{A}}\right)}{\left(1 + \varepsilon X_{\text{A}} + \gamma\right)} \quad \text{.....(11)}$$

$$C_{\text{A}} = y_{\text{A}} C_{\text{T}} \quad \text{.....(12)}$$

Additionally, the power rate law as expressed in Eq. **Error! Reference source not found.**, was used to evaluate the reaction rate $(-r_{\text{A}})$, order of reaction (n), and rate constant (k_{A}).

$$-r_A = k_A C_A^n \quad \text{.....(13)}$$

The first derivative of the polynomial equation obtained from plotting (X_A) against (V_{cat} / F_A) would allow for the determination of the order of reaction while the expanded logarithmic form of Eq. **Error! Reference source not found.**, shown in Eq. **Error! Reference source not found.**, would produce the values of the order of reaction and subsequent rate constant (Froment et al., 2010).

$$\log\left(-r_A\right) = \log k_A + n \log C_T + n \log\left(\frac{1 - X_A}{1 + \varepsilon X_A + \gamma}\right) \quad \text{.....(14)}$$

Reaction Mechanism of a Catalyzed Reaction

As illustrated in Figure 1, several steps occur in a heterogeneously catalyzed reaction: Diffusion of reactants from the bulk fluid to the surface of the catalyst particle (1); Pore or intra-particle diffusion (2); Reactants are absorbed by the catalyst (3); Catalytic reaction at the catalyst's active sites (4); Catalytic product desorption (5); Transportation of reaction products from the solid catalyst's interior to its exterior pore mouth (6), and; Transport of the products of reaction from the pellet's surface to the surrounding fluid (7) (Raweewan et al., 2011).

In theoretical studies, analysis of transport limitations makes use of various dimensionless numbers from the field of transport phenomena. The evaluation of internal and external mass transfer limitations is crucial to the simulation, design, and modeling of heterogeneous reaction processes; thus, the determination of Thiele modulus, effectiveness factor, overall effectiveness factor, mass transfer coefficient, and all other unknown parameters is essential. Since Thiele's (Thiele, 1939) seminal 1939 study detailing the influence of particle size on catalyst activity, numerous studies on mass transfer have reported determining the effectiveness factor (Talebian-Kiakalaieh & Amin, 2016). Experimentally, the reactant conversion is observed while varying both particle size and feed flow rate.

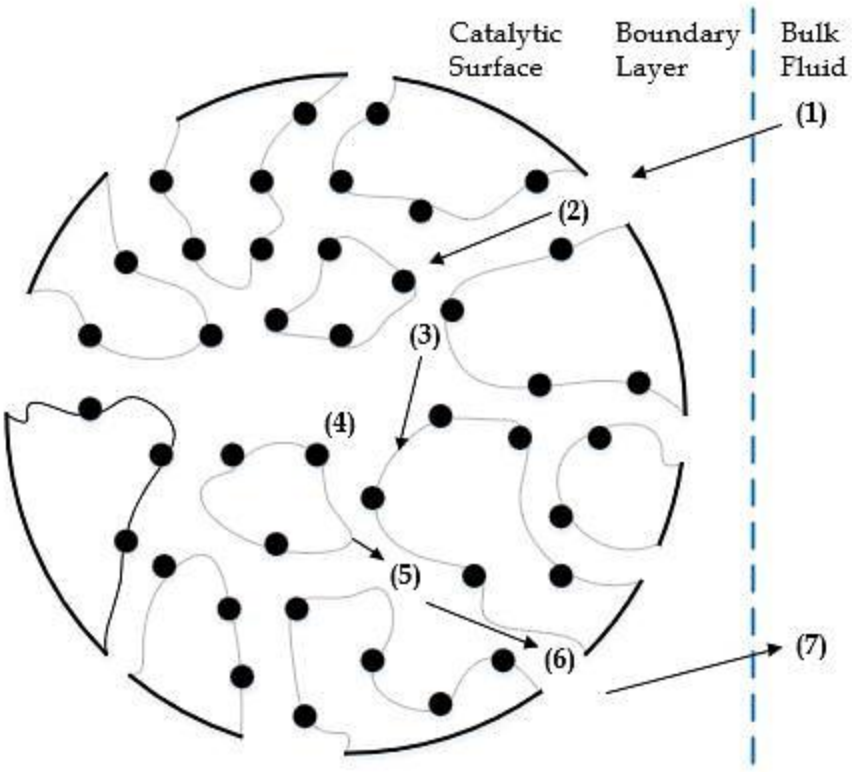

Figure 1. Heterogeneous catalytic reaction mechanism

Theoretical Approaches to Transport Limitation Assessment

Theoretically, the gas phase and intra-particle transport limitation assessment were conducted by evaluating the Mears' and Weisz Prater criteria. The procedure in itself involved the determination of various parameters linked to transport phenomena. Initially, Using the Wilke-Chang equation, Eq. **Error! Reference source not found.**, the coefficient of diffusion (D_{AB}) was calculated. This coefficient, commonly known as diffusivity, is a constant proportional to the ratio of the concentration gradient of the species to the molar flow owing to molecular diffusion (Miyabe & Isogai, 2011).

$$D_{AB} = \frac{7.4\times10^{-8} T\sqrt{\theta_B M_B}}{\mu V_A^{0.6}} \quad \text{.....(15)}$$

Where (θ_B) is the solvent's "association parameter" (a dimensionless quantity = 2.6 for H2O) (Gemo et al., 2012), (M_B) is the molar mass of the solvent B (which is H2O for the current study), (μ) is the solution's dynamic viscosity and (V_A) is the molar volume of the solute A (ethanol) at its boiling temperature (Delidovich et al., 2013; Le Bas, 1915). Next, the Knudsen diffusivity (D_{KA}) was determined by solving Eq. **Error! Reference source not found.**, which takes into consideration the collisions that occur between molecules and the pore walls

.

$$D_{\mathrm{KA}} = \left(9.7\times10^{3}\right)\cdot R_{\mathrm{pore}}\cdot\left(\frac{T}{M_{\mathrm{A}}}\right)^{1/2} \quad \text{.....(16)}$$

In this case, $\left(R_{\mathrm{pore}}\right)$ is catalytic pellet pore size (radius) and $\left(M_{\mathrm{A}}\right)$ is the molecular weight of ethanol. To investigate the typical regions of the vacuum in the Knudsen, transition, and molecular diffusion regimes, the effective transition diffusivity $\left(D^{\mathrm{e}}_{\mathrm{TA}}\right)$ was computed using the Bosanquet equation, Eq. **Error! Reference source not found.**. Here, $(D^{\mathrm{e}}_{\mathrm{AB}})$ is effective diffusivity and $(D^{\mathrm{e}}_{\mathrm{KA}})$ is effective Knudsen diffusivity, which were computed using Eq. **Error! Reference source not found.**.

$$\frac{1}{D^{\mathrm{e}}_{\mathrm{TA}}} = \frac{1}{D^{\mathrm{e}}_{\mathrm{AB}}} + \frac{1}{D^{\mathrm{e}}_{\mathrm{KA}}} \quad \text{.....(17)}$$

$$D^{\mathrm{e}}_{\mathrm{AB}} = \frac{\varepsilon_{\mathrm{p}}}{\tau}\cdot D_{\mathrm{AB}} \quad \text{and} \quad D^{\mathrm{e}}_{\mathrm{KA}} = \frac{\varepsilon_{\mathrm{p}}}{\tau}\cdot D_{\mathrm{KA}} \quad \text{.....(18)}$$

In the calculation of both effective and effective Knudsen diffusivity, two new parameters are introduced, $\left(\varepsilon_{\mathrm{p}} \text{ and } \tau\right)$. $(\varepsilon_{\mathrm{p}})$ is pellet porosity (void space volume as a fraction of total volume, $(\text{Pore volume } (V_{\mathrm{pore}}) / \text{ Total volume of catalyst bed } (V_{\mathrm{cat}}))$). Respectively, (τ) is tortuosity (distance a molecule actually travels between two sites compared to the smallest distance that could be travelled by the molecule) and was calculated from ($\tau = 1 - 0.5\ln(\varepsilon)$) (Geankoplis et al., 2018).

.

Gas-Phase Mass Transport Limitation

To evaluate external diffusion limitations, the Thoenes-Kramers correlations were used to determine parameters including; linear superficial fluid velocity (u) and the dimensionless Reynolds $\left(Re'\right)$, Schmidt $\left(Sc\right)$, and Sherwood number $\left(Sh'\right)$ as per Eqs. **Error! Reference source not found.**, **Error! Reference source not found.**, **Error! Reference source not found.** and **Error! Reference source not found.** (Roberts, 2008)

$$u = \frac{v_0}{A_{\mathrm{c}}} \quad \text{.....(19)}$$

$$Re' = \frac{u\cdot d_{\mathrm{p}}}{\left(1-\varphi\right)\cdot\upsilon} \quad \text{.....(20)}$$

$$Sc = \frac{\bar{\mu}}{\rho D_{\mathrm{AB}}} = \frac{\upsilon}{D_{\mathrm{AB}}} \quad \text{.....(21)}$$

$$Sh' = (Re')^{1/2}\cdot(Sc)^{1/3} \quad \text{.....(22)}$$

Where; (v_0) is the reactant volumetric flow rate, (A_c) is the tubular reactor cross-section area, $(\bar{\mu})$ is the kinematic viscosity, and (ρ) is the ethanol/water mixture density at reactor operating conditions of temperature and pressure. The mass transfer coefficient (k_c), a parameter that quantifies mass transport between the fluid and the porous solid in heterogeneous catalysis, was calculated using Eq. **Error! Reference source not found.**, where (φ) is catalyst bed porosity.

$$k_c = \frac{1-\varphi}{\varphi}.\left(\frac{D_{AB}}{d_p}\right) \cdot Sh' \quad \text{.....(23)}$$

Ultimately, Mears' Criterion states that if the criterion in Eq. **Error! Reference source not found.** is met, the restrictions of interphase mass transfer do not significantly affect the predicted reaction rate. Here, $\left(-r_A^{'}\rho_b\right)$ is the measured reaction rate, $\left(R_p\right)$ is the catalyst pellet radius, (n) is reaction order and $\left(C_{Ab}\right)$ is the concentration of ethanol (A) in the bulk fluid (Davis & Davis, 2013)

.

$$\frac{\left(-r_A^{'}\rho_b\right)R_p n}{k_c C_{Ab}} < 0.15 \quad \text{.....(24)}$$

Intra-Particle Mass Transport Constraint

Whether or not internal mass transport limitations are present can be determined using the Weisz-Prater criterion, by computing Eq. **Error! Reference source not found.** and examining the satisfaction of the conditions outlined in Eq. **Error! Reference source not found.**.

$$C_{WP} = \eta\phi_n^2 = 3\left(\phi_n \cdot \coth\phi_n - 1\right) \quad \text{.....(25)}$$

$$C_{WP} = \frac{\text{Observed Reaction Rate}}{\text{Rate as per Diffusion}} << 1, \text{ no internal diffusion} \quad \text{.....(26)}$$

$$C_{WP} = \frac{\text{Observed Reaction Rate}}{\text{Rate as per Diffusion}} >> 1, \text{ internal diffusion exists}$$

In the valuation of $\left(C_{WP}\right)$, (η) represents the rate of reaction inside the pellet as a fraction of that on the pellet's surface; also known as the internal effectiveness factor, which was calculated using Eq. **Error! Reference source not found.**. $\left(\phi_n\right)$ is the Thiele modulus, respectively calculated using Eq. **Error! Reference source not found.**. From literature, if the value of the Thiele modulus is high, there are more intra-particle mass transport (Hill & Root, 2014). $\left(C_{As}\right)$ is the external surface ethanol concentration on the catalyst and $(\psi\left(\text{reversibility factor}\right)=1)$ for irreversible reactions, as is the case for gas-phase conversion of ethanol.

$$\eta = \frac{\tanh(\phi_n)}{\phi_n} \quad \text{.....(27)}$$

$$\phi_n = L_p\left(\frac{\left(n+1\right)\cdot k_n \cdot C_{As}^{n-1}}{2D_{TA}^{e}}\right)^{1/2} \cdot \psi \quad \text{.....(28)}$$

The particle size dependency of the Thiele modulus is distinguished by the characteristic length (L_p), itself, a function of pellet volume (V_p) and surface area (S_p), and can be modeled, for spherical pellets, as per Eq. **Error! Reference source not found.**.

$$L_p = \frac{V_p}{S_p} = \frac{R_p}{3} \quad \text{.....(29)}$$

Overall effectiveness factor

Large values of the interphase mass transport coefficient (k_c) are observed from high flow rates, as was the case in this investigation. In such a scenario, the effectiveness factor approaches the internal effectiveness factor, Eq.).

$$\Omega \cong \eta \quad \text{.....(30)}$$

Experimental Approaches to Transport Limitation Assessment

Intra-particle mass transport limitation

To investigate intra-particle mass transfer resistance or absence of the same, the reaction conversion rate is observed for catalyst pellets of different diameters (d_p), while keeping the mass of the catalyst bed and contact time constant. As illustrated in **Figure 2**, small catalyst pellets exhibit high and stabilized constant conversion of reactant, since internal diffusion would not limit the reaction rate (Bej et al., 2014). The presence or absence of intra-particle mass transport resistance was tested by conducting ethanol conversion to hydrogen experiments with heterogeneous catalysts of two distinct particle sizes.

The conversion of ethanol over $Ni_{0.12}$-$MMT_{0.20}$/TMPs and $Ni_{0.12}$-$MMT_{0.20}$/TNPs was monitored.

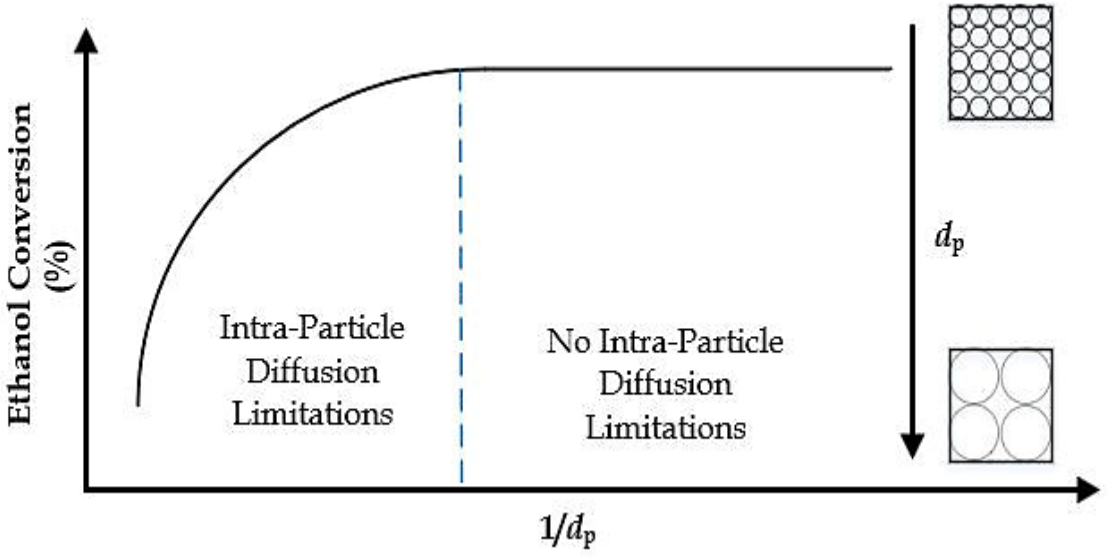

Figure 2. Experimental assessment of intra-particle diffusion limitation

Gas-phase mass transport limitation

The existence of mass transport resistance in the gas phase was measured by increasing the space-time (W/F, the mass of catalyst/ reactant molar flow rate) at isothermal reactor conditions while maintaining a constant catalyst particle size ($Ni_{0.12}$-$MMT_{0.20}$/TNPs). The non-existence of gas-phase mass transport limitations can be inferred from the fact that the rate of ethanol conversion is constant across different spacetimes, (Ballari et al., 2008), (Figure 3).

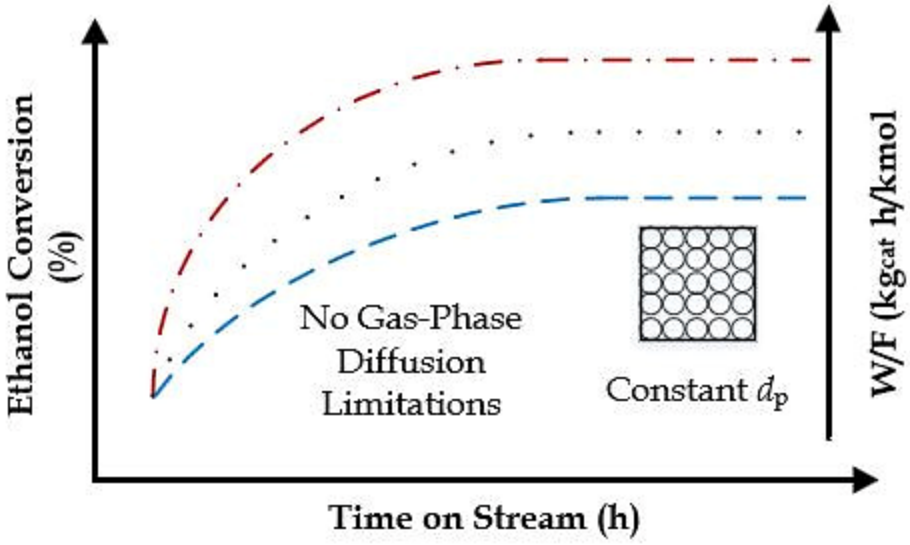

Figure 3. Experimental assessment of gas-phase diffusion limitation

Results and Discussion

Micro and Nanoparticle Catalysts Characterization

The XRD patterns of the $Ni_{0.12}$-$MMT_{0.20}$/TMP and $Ni_{0.12}$-$MMT_{0.20}$/TNP catalysts are shown in **Figure 4a**. Similar peaks were seen in the diffractions, with 2 theta peaks that agreed with the associated planes of Titania's tetragonal anatase structure (Mulewa et al., 2017a). When compared to microparticles, the nanoparticles had a somewhat broader TiO_2 peak 101, suggesting a smaller crystallite size. In addition, MMT peak 001 is nonexistent because MMT is efficiently dispersed on TiO_2 particles. The average crystallite diameter of Ni-MMT/TiO_2-NPs was 11.34 nm with a lattice strain of 0.0149, obtained from Scherer's equation. calculated using Scherrer's equation $\left(D_p = K\lambda / \beta_{1/2}\cos\theta\right)$ (Mansor et al., 2018). Next, the calcined and reduced Ni-MMT/TiO_2-NPs were subjected to FTIR analysis where quite similar spectra were observed, (Figure 4b). The 3631 peak is associated with the stretching vibration of the hydroxyl bond, whereas the 1640 peak is associated with C=O vibrations. Both the 1042 peak and the 918 peaks may be associated with hydroxyl groups in water molecules. Ti-O vibrations are represented by little peaks in the curve near 550 cm^{-1}.

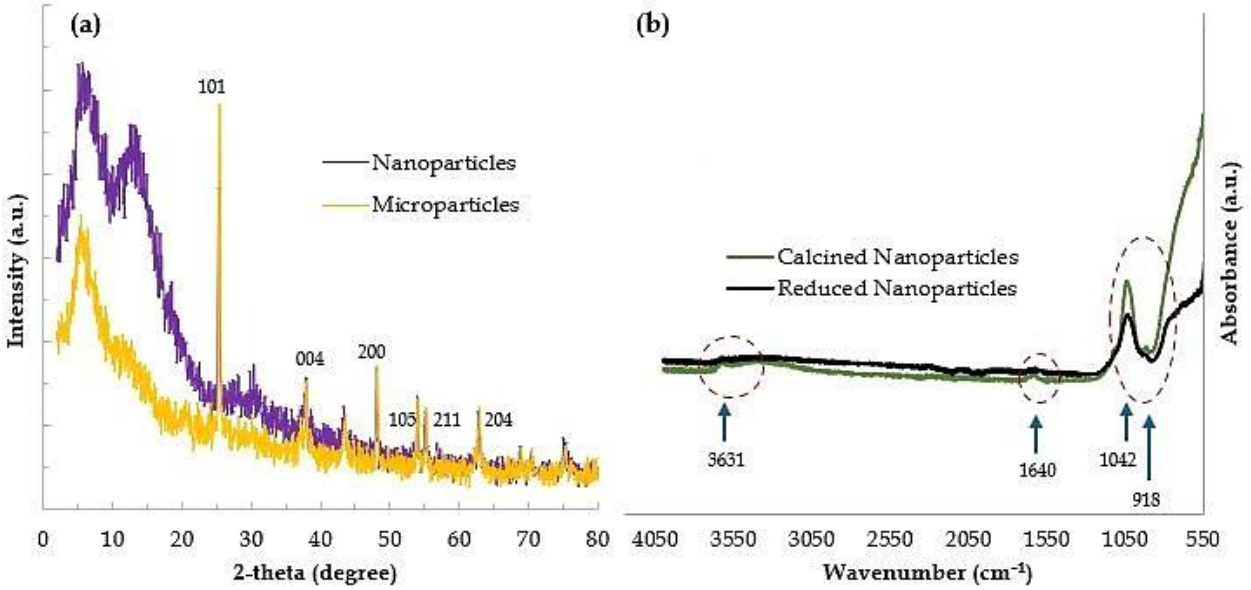

Figure 4 (a) MPs and NPs XRD patterns (b) FTIR spectra of calcined and reduced NPs

As shown in Figure **5**, SEM and EDX were used to examine the nanoparticles' morphology and microscopic structure. Figure 5a shows that the TiO_2 particles were almost spherical and uniform in size, as determined by scanning electron microscopy. The MMT sheets are likewise visible, but the Ni is unidentifiable. This is likely because Ni has such a low weight percentage on the catalyst and is so evenly distributed on the MMT sheets.

The physicochemical characteristics of $Ni_{0.12}$-$MMT_{0.20}$/TNPs are summarized next to the corresponding SEM micrograph. Figure 5b is the EDX mapping, evidently showing a consistent Ni coverage of the MMT/TiO_2 substrate, an indication of successful modified sol-gel synthesis of the catalyst

.

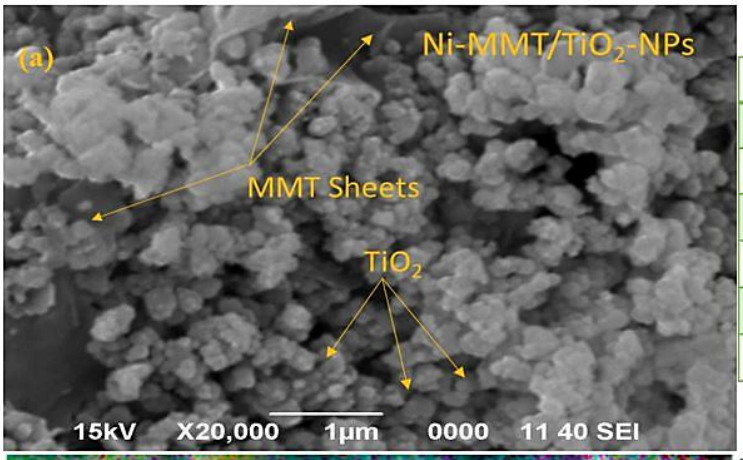

Ni-MMT/TiO_2-NPs	
BET surface area (m^2/g)	15.38
BJH surface area (m^2/g)	8.77
t-plot, micro-pore area (m^2/g)	10.47
BJH pore volume (cm^3/g)	0.112
t-plot micro-pore volume (cm^3/g)	0.0043
BJH pore width (nm)	5.12

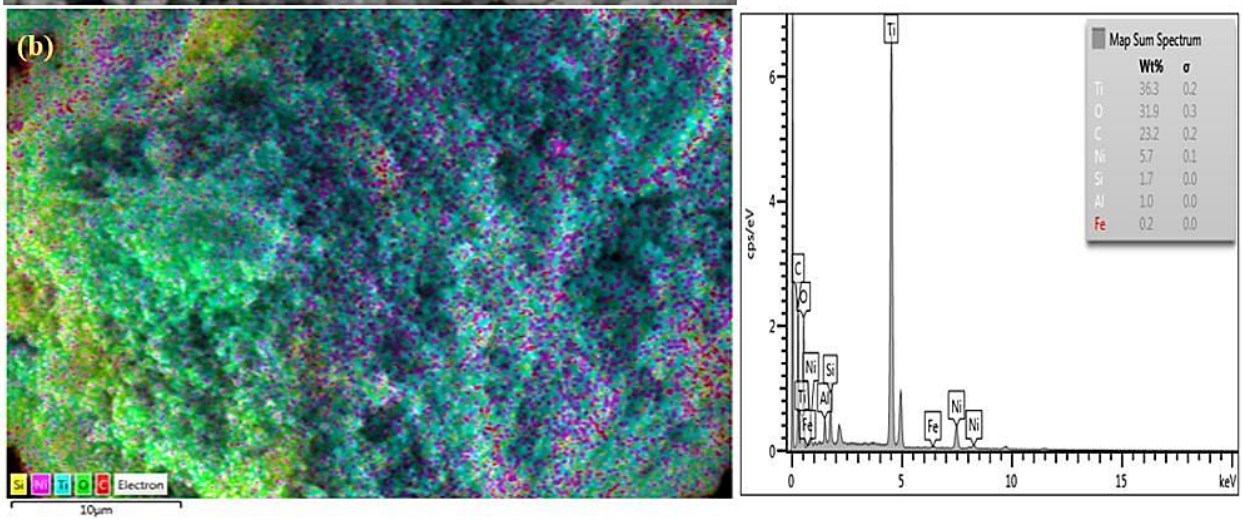

Figure 5. (a) Scanning Electron Micrographs of Ni0.12-MMT0.20/TNPs and corresponding Physico-chemical properties, (b) Energy Dispersive X-ray mapping of Ni0.12-MMT0.20/TNPs

Figure 6a shows the N_2 adsorption/desorption isotherms for the calcined nanoparticles, which are typical hysteresis loop-type (type IV) curves for porous materials. The pore diameter ranges from 5.45-277.38 nm (Figure 6b), Barrett-Joyner-Halenda (BJH) isotherms for the distribution of pore sizes), with a central value of 17.5 nm. As can be seen, most particles are less than 50 nm in diameter. This indicates that tiny pores are produced during the impregnation and structural alteration of TiO_2, most likely because of the presence of MMT. $Ni_{0.12}$-$MMT_{0.20}$/TNPs also have a larger Ni dispersion because their smaller pores help to avoid agglomeration (Lee et al., 2013).

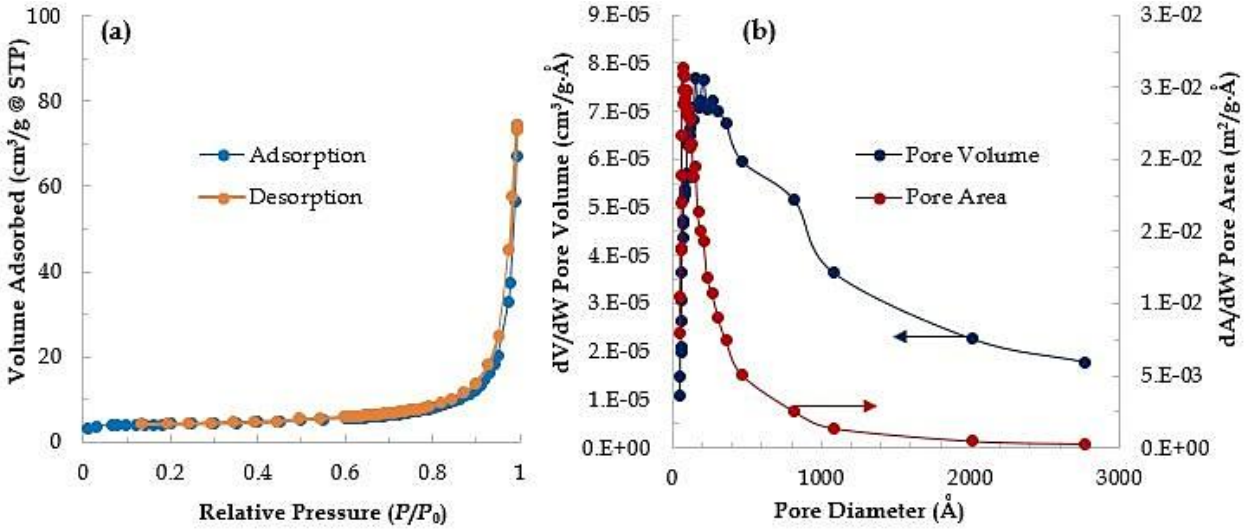

Figure 6. (a) Isotherms of nitrogen dioxide adsorption and desorption, (b) Isotherms for the pore size distribution of the nanoparticle catalyst.

Kinetic Parameters

Conversion of ethanol is highly dependent on space-time as seen in Figure **7**. The first derivative of the second-order polynomial $(-0.4088x + 0.699)$ obtained from the plot allowed for the calculation of the reaction rate $(-r_A)$ at a given (V_{cat}/F_A) and reaction temperature

.

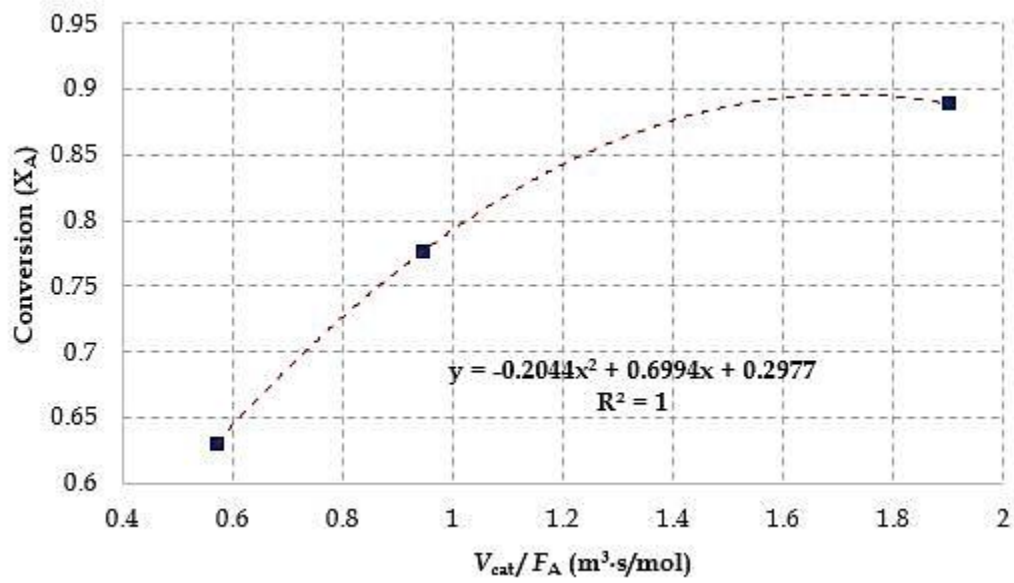

Figure 7. Ethanol Conversion (XA) versus Reactants Space-Time (Vcat/FA)

From the slope and intercept, Eq. **Error! Reference source not found.** was used to determine the rate constant and reaction order by varying the temperature parameter of the experiment and plotting the values $(\log(-r_A))$ against those of $((1-X_A)/(1+\varepsilon_A X_A+\gamma))$, Figure 8 (a & b). From the plots, it can be deduced

that the reaction order for ethanol was approximately 0.76, hence the rate law would be expressed as $\left(-r = kC_{\text{ethanol}}^{0.76},\ \text{mol/m}^3\cdot\text{s}\right)$. For the reaction temperature of 500 °C, the value of the rate constant was found to be 699 $(\text{mol/m}^3)^{0.24}\cdot\text{s}^{-1}$. The high value of the rate constant signifies that EtOH can be quickly converted to H_2 by a gas-phase conversion process (Levenspiel, 2019).

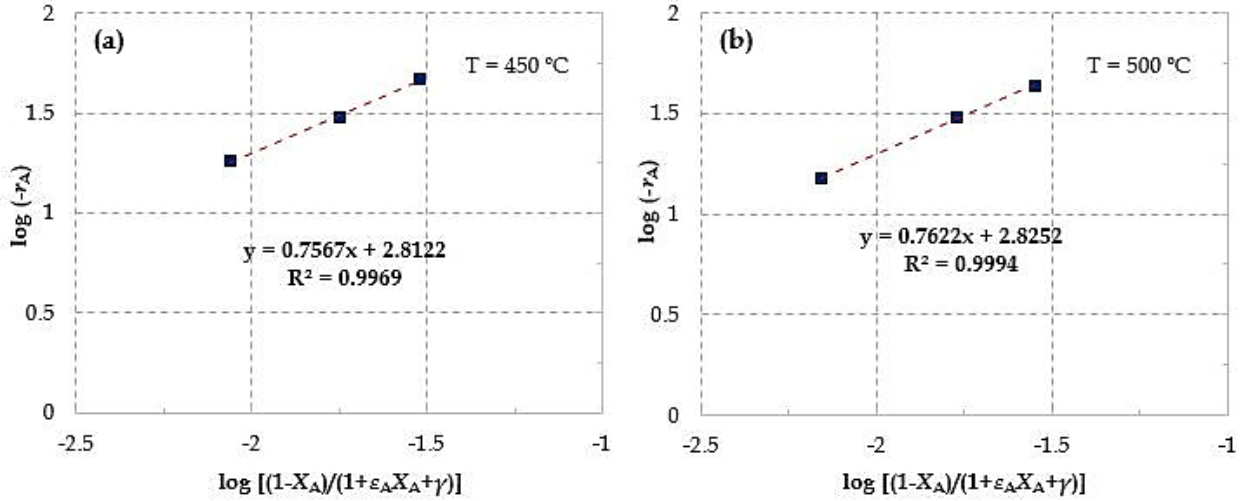

Figure 8. Log (-rA) versus log((1-XA)/(1+εAXA+γ) for two evaluated temperatures: (a) 450 °C and (b) 500 °C.

Theoretical Approach

Gas-Phase Transport Constraint

The calculated values of pellet porosity and tortuosity were $\left(\varepsilon_p = 0.046\right)$ and $\left(\tau = 2.545\right)$ respectively. These values allowed for the computation of an effective diffusivity of $D_{TA}^{e} = 2.02\times10^{-9}\ \text{m}^2/\text{s}$. The TPBR had a flow cross-sectional area $\left(A_c = 5.027\times10^{-5}\ \text{m}^2\right)$ with a reactant volumetric flow rate $\left(\nu_0 = 6.667\times10^{-7}\ \text{m}^3/\text{s}\right)$ and superficial velocity $\left(U = 1.326\times10^{-2}\ \text{m/s}\right)$. Additionally, the kinematic viscosity $\left(\upsilon = 9.165\times10^{-5}\ \text{m}^2/\text{s}\right)$ was computed from the dynamic viscosity and density of the solution at the reaction temperature of 500 °C.

Having determined the pre-requisite parameters, the values of $\left(Re', Sc, Sh' \text{ and } k_c\right)$ and valuation of Mears' criterion $\left(MC\right)$ at various pellet diameters are summarized in Table 1. The results confirmed that at the given reactor conditions, catalyst pellets $\left(d_p < 9\ \mu\text{m}\right)$ would not be susceptible to gas-phase mass transport limitations.

Table 1. Parameters for Valuation of Mears' Criterion

No.	$d_p\ (\mu\text{m})$	$Re'\left(10^{-4}\right)$	Sc	Sh'	$k_c\ (\text{m/s})$	(MC)
1	2	3.858	811.036	0.182	0.031	0.017
2	4	7.716	811.036	0.258	0.022	0.048
3	6	11.574	811.036	0.317	0.018	0.089
4	8	15.433	811.036	0.366	0.015	0.137
5	9	17.362	811.036	0.388	0.014	0.164
6	20	38.582	811.036	0.578	0.010	0.542
7	40	77.163	811.036	0.817	0.007	1.533

Constraints on Mass Transport Inside Particles and Their Effect on Efficiency

Intra-particle mass transport limitation assessment aimed to find the spherical geometry particle diameter size that marked the boundary of the WPC of internal mass transfer diffusion, Eq. **Error! Reference source not found.**. As previously reported, the calculated constant for the rate of reaction was $\left(k_{0.76} = 699\ \left(\text{mol/m}^3\right)^{0.24} \cdot \text{s}^{-1}\right)$ at the reaction temperature of 500 °C. For various pellet diameters, the Thiele modulus (ϕ_n), effectiveness (η), and overall effectiveness (Ω) factors were calculated and respective values were presented in Table 2. Theoretically, no internal diffusion would be observed for catalyst pellets $\left(d_p < 6\ \mu\text{m}\right)$. This can be attributed to high effectiveness $(\eta > 0.9)$ and the fact that $(C_{WP} \square\ 1)$. However, when extended to larger particles, $\left(\text{for } d_p = 40\ \mu\text{m},\ \eta = 0.330 \text{ and } C_{WP} = 7.395 \square\ 1\right)$ internal diffusion was found to limit the reaction rate.

Table 2. Parameters for valuation of Weisz-Prater Criterion

No.	$d_p\ (\mu\text{m})$	$\phi_{0.76}$	$\eta \cong \Omega$	C_{WP}
1	1	0.198	0.997	0.039
2	2	0.397	0.989	0.149
3	4	0.793	0.960	0.524
4	6	1.190	0.917	0.989
5	7	1.389	0.891	1.226
6	20	3.967	0.566	3.965
7	40	7.935	0.330	7.395

Figuratively, ethanol gas-phase conversion over catalyst pellets $\left(d_p < 6\ \mu\text{m}\right)$ would only be reaction-limited due to the absence of intra-particle transport limitations, Figure 9a. .

Moreover, the relationship between effectiveness and pellet diameter is illustrated in Figure 9b. Summarily, smaller catalyst pellets are more effective comparatively.

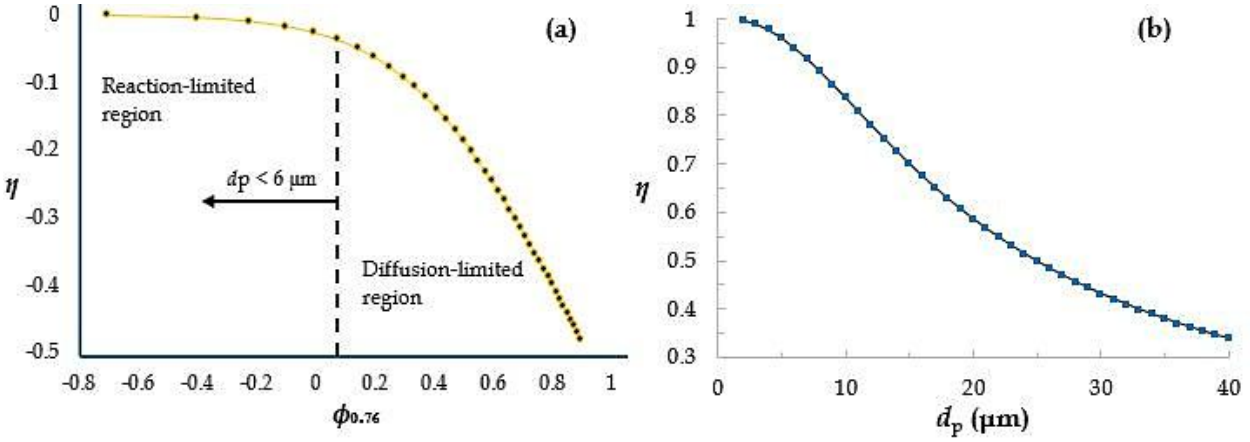

Figure 9. (a) η *versus* ϕn (log-log plot), (b) Effectiveness versus particle size

Experimental Approach to Intra-particle and gas-phase transport Limitations

Further experimental analysis was performed on mass transport restrictions to correlate diffusion limitations with catalyst physicochemical parameters. The presence or absence of intra-particle mass transport resistance was analyzed by varying the catalyst pellet sizes while maintaining reactor conditions temperature (500 ^{o}C), pressure (atmospheric), and feed flow rate (2 mL/h). Ethanol conversion for microparticles and nanoparticles was compared. Observing Figure 10, the very identical ethanol conversion curves show that EtOH conversion took place in the resistance-free zone of intra-particle mass transport.

This indicates that the concentration on the catalyst surface is equivalent to the concentration within its pores and that, within the pellet, there are no concentration variations. This is because there are no internal barriers preventing diffusion through the pores (Lattanzi et al., 2020).

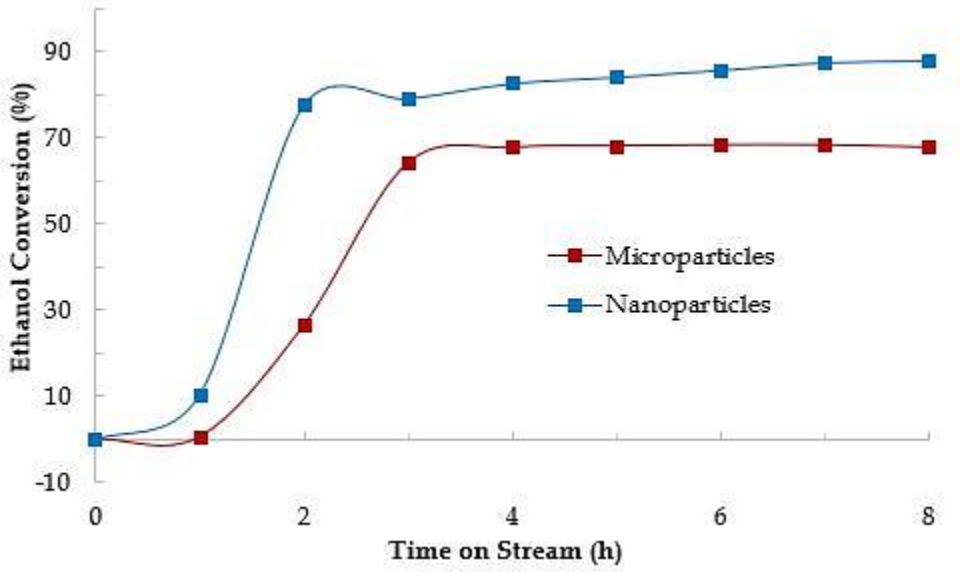

Figure 10. Ethanol conversion over time for micro and nanoparticles

Ultimately, the mass of the catalyst bed was held constant, and the space times were adjusted by varying the reactant supply of the gas-phase EtOH/H_2O mixture. Space-time effects on ethanol conversion were studied while keeping the pellet size of the catalyst constant (nanoparticles). As illustrated in Figure 11, because there is no hindrance to mass transport, consistent trends for ethanol conversion were observed across a wide range of spacetimes (W/F).

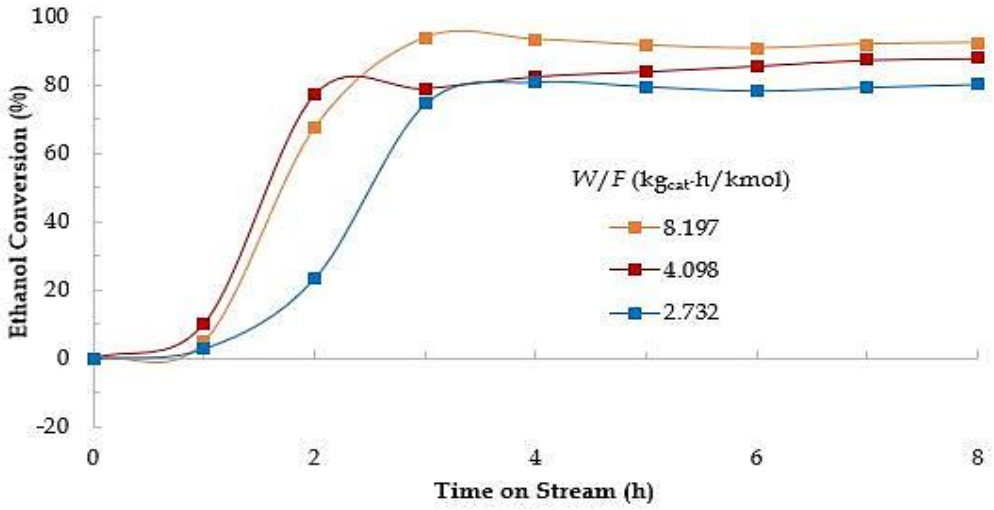

Figure 11. Conversion of ethanol and the effect of space-time on nanoparticle catalyst

Conclusions

The existence or absence of gas-phase and intra-particle transport limitations in gaseous ethanol conversion to hydrogen over a $Ni_{0.12}$-$MMT_{0.20}$/TNP catalyst were investigated at a temperature of 500 ^{o}C under atmospheric conditions of pressure in a tubular packed bed reactor (TPBR). Both theoretical and experimental results confirmed that the nanoparticle catalyst was not constrained by gas-phase or intra-particle transport limitations. This is because the Montmorillonite/Titania support, with its nano-scale particle size, enhances Ni dispersion and provides an abundance of redox sites on the catalyst surface, making the EtOH/H_2O mixture more amenable to reduction. According to the findings, pellet sizes of 6-8 µm would allow for optimal catalyst use under the specified circumstances of the reactor. At all space times, feed molar ratios, and temperatures, H_2 is the primary product. Additionally, EtOH decomposition, and steam reforming processes all work in tandem to favor a high conversion rate, selectivity for H_2, and yield with increasing temperature.

Acknowledgment

To support this study, the authors wish to express utmost gratitude to the Technical University of Mombasa's Office of Partnerships, Research, and Innovation (PRI).

References

Ballari, M. d. l. M., Brandi, R., Alfano, O., & Cassano, A. (2008). Mass transfer limitations in photocatalytic reactors employing titanium dioxide suspensions: II. External and internal particle constrains for the reaction. *Chemical Engineering Journal, 136*(2), 242-255. doi:https://doi.org/10.1016/j.cej.2007.03.031

Davis, M. E., & Davis, R. J. (2013). *Fundamentals of Chemical Reaction Engineering* (2 ed.): Dover Publications.

Delidovich, I. V., Moroz, B. L., Taran, O. P., Gromov, N. V., Pyrjaev, P. A., Prosvirin, I. P., . . . Parmon, V. N. (2013). Aerobic selective oxidation of glucose to gluconate catalyzed by Au/Al_2O_3 and Au/C: Impact of the mass-transfer processes on the overall kinetics. *Chemical Engineering Journal, 223*, 921-931. doi:https://doi.org/10.1016/j.cej.2012.11.073

Deluga, G. A., Salge, J. R., Schmidt, L. D., & Verykios, X. E. (2004). Renewable Hydrogen from Ethanol by Autothermal Reforming. *Science, 303*(5660), 993-997. doi:doi:10.1126/science.1093045

Fogler, H. S. (2016). *Elements of Chemical Reaction Engineering* (2 ed.): Prentice Hall.

Froment, G. F., Bischoff, K. B., & De Wilde, J. (2010). *Chemical Reactor Analysis and Design* (3 ed.): John Wiley & Sons, Incorporated.

Gemo, N., Biasi, P., Canu, P., & Salmi, T. O. (2012). Mass transfer and kinetics of H_2O_2 direct synthesis in a batch slurry reactor. *Chemical Engineering Journal, 207-208*, 539-551. doi:https://doi.org/10.1016/j.cej.2012.07.015

Graschinsky, C., Giunta, P., Amadeo, N., & Laborde, M. (2012). Thermodynamic analysis of hydrogen production by autothermal reforming of ethanol. *International Journal of Hydrogen Energy, 37*(13), 10118-10124. doi:https://doi.org/10.1016/j.ijhydene.2012.01.182

Gullapelli, S., Scurrell, M. S., & Valluri, D. K. (2017). Photocatalytic H_2 production from glycerol–water mixtures over Ni/γ-Al_2O_3 and TiO_2 composite systems. *International Journal of Hydrogen Energy, 42*(22), 15031-15043. doi:https://doi.org/10.1016/j.ijhydene.2017.04.239

Heard, B. P., Brook, B. W., Wigley, T. M. L., & Bradshaw, C. J. A. (2017). Burden of proof: A comprehensive review of the feasibility of 100% renewable-electricity systems. *Renewable and Sustainable Energy Reviews, 76*, 1122-1133. doi:https://doi.org/10.1016/j.rser.2017.03.114

Hou, T., Zhang, S., Chen, Y., Wang, D., & Cai, W. (2015). Hydrogen production from ethanol reforming: Catalysts and reaction mechanism. *Renewable and Sustainable Energy Reviews, 44*, 132-148. doi:https://doi.org/10.1016/j.rser.2014.12.023

Hussein, A. (2023). Chapter 1 - Oil and Gas Production Operations and Production Fluids. In A. Hussein (Ed.), *Essentials of Flow Assurance Solids in Oil and Gas Operations* (pp. 1-52): Gulf Professional Publishing.

Kraleva, E., Pohl, M.-M., Jürgensen, A., & Ehrich, H. (2015). Hydrogen production by bioethanol partial oxidation over Ni based catalysts. *Applied Catalysis B: Environmental, 179*, 509-520. doi:https://doi.org/10.1016/j.apcatb.2015.06.004

Lattanzi, A. M., Pecha, M. B., Bharadwaj, V. S., & Ciesielski, P. N. (2020). Beyond the effectiveness factor: Multi-step reactions with intraparticle diffusion limitations. *Chemical Engineering Journal, 380*, 17. doi:https://doi.org/10.1016/j.cej.2019.122507

Le Bas, G. (1915). *The Molecular Volumes Of Liquid Chemical Compounds, From The Point Of View Of Kopp*. London: Longmans, Green and Company.

Lee, J.S., Choi, J.-P., & Lee, G.-Y. (2013). Consolidation of Hierarchy-Structured Nanopowder Agglomerates and Its Application to Net-Shaping Nanopowder Materials. *Materials, 6*(9), 4046-4063. doi:10.3390/ma6094046

Levenspiel, O. (2019). *Chemical Reaction Engineering* (3 ed.): Wiley.

Liu, Q., Zhou, H., & Jia, Z. (2022). Hydrogen Production by Ethanol Reforming on Supported Ni–Cu Catalysts. *ACS Omega, 7*(5), 4577-4584. doi:10.1021/acsomega.1c06579

Mansor, M. R., Mustafa, Z., Fadzullah, S. H. S. M., Omar, G., Salim, M. A., & Akop, M. Z. (2018). 3 - Recent Advances in Polyethylene-Based Biocomposites. In S. M. Sapuan, H. Ismail, & E. S. Zainudin (Eds.), *Natural Fibre Reinforced Vinyl Ester and Vinyl Polymer Composites* (pp. 71-96): Woodhead Publishing.

Megía, P. J., Vizcaíno, A. J., Calles, J. A., & Carrero, A. (2021). Hydrogen Production Technologies: From Fossil Fuels toward Renewable Sources. A Mini Review. *Energy & Fuels, 35*(20), 16403-16415. doi:10.1021/acs.energyfuels.1c02501

Mielenz, J. R. (2001). Ethanol production from biomass: technology and commercialization status. *Current Opinion in Microbiology, 4*(3), 324-329. doi:https://doi.org/10.1016/S1369-5274(00)00211-3

Miyabe, K., & Isogai, R. (2011). Estimation of molecular diffusivity in liquid phase systems by the Wilke–Chang equation. *Journal of Chromatography A, 1218*(38), 6639-6645.

doi:https://doi.org/10.1016/j.chroma.2011.07.018

Mulewa, W., Tahir, M., & Amin, N.A.S. (2017a). Ethanol Steam Reforming for Renewable Hydrogen Production over La-modified Tio_2 Catalyst. *Chemical Engineering Transactions, 56*, 349-354. doi:10.3303/CET1756059

Mulewa, W., Tahir, M., & Amin, N.A.S. (2017b). MMT-supported Ni/TiO_2 nanocomposite for low temperature ethanol steam reforming toward hydrogen production. *Chemical Engineering Journal, 326*, 956-969. doi:https://doi.org/10.1016/j.cej.2017.06.012

Muradov, N. (2017). Low to near-zero CO_2 production of hydrogen from fossil fuels: Status and perspectives. *International Journal of Hydrogen Energy, 42*(20), 14058-14088. doi:10.1016/j.ijhydene.2017.04.101

Pafili, A., Charisiou, N. D., Douvartzides, S. L., Siakavelas, G. I., Wang, W., Liu, G., . . . Goula, M. A. (2021). Recent Progress in the Steam Reforming of Bio-Oil for Hydrogen Production: A Review of Operating Parameters, Catalytic Systems and Technological Innovations. *Catalysts, 11*(12), 34. doi:https://doi.org/10.3390/catal11121526

Ranjekar, A. M., & Yadav, G. D. (2021). Steam Reforming of Methanol for Hydrogen Production: A Critical Analysis of Catalysis, Processes, and Scope. *Industrial & Engineering Chemistry Research, 60*(1), 89-113. doi:10.1021/acs.iecr.0c05041

Raweewan, K., Matthias, A., & Wolfgang, F. H. (2011). A Review of Mass Transfer Controlling the Reaction Rate in Heterogeneous Catalytic Systems. In N. Hironori (Ed.), *Mass Transfer* (pp. 20). Rijeka: IntechOpen.

Roberts, G. W. (2008). *Chemical Reactions and Chemical Reactors* (Illustrated Ed.): John Wiley & Sons.

Sahoo, S., Dekel, D. R., Maric, R., & Alpay, S. P. (2021). Atomistic Insights into the Hydrogen Oxidation Reaction of Palladium-Ceria Bifunctional Catalysts for Anion-Exchange Membrane Fuel Cells. *ACS Catalysis, 11*(5), 2561-2571. doi:10.1021/acscatal.0c04646

Sawatmongkhon, B., Theinnoi, K., Wongchang, T., Haoharn, C., Wongkhorsub, C., & Tsolakis, A. (2019). Hydrogen Production via the Catalytic Partial Oxidation of Ethanol on a Platinum–Rhodium Catalyst: Effect of the Oxygen-to-Ethanol Molar Ratio and the Addition of Steam. *Energy & Fuels, 33*(7), 6742-6753. doi:10.1021/acs.energyfuels.9b01398

Shin, S.A., Alizadeh Eslami, A., Noh, Y.S., Song, H.-t., Kim, H.D., Ghaffari Saeidabad, N., & Moon, D. J. (2020). Preparation and Characterization of $Ni/ZrTiAlO_x$ Catalyst via Sol-Gel and Impregnation Methods for Low Temperature Dry Reforming of Methane. *Catalysts, 10*(11), 22. doi:10.3390/catal10111335

Sun, S., Yan, W., Sun, P., & Chen, J. (2012). Thermodynamic analysis of ethanol reforming for hydrogen production. *Energy, 44*(1), 911-924. doi:https://doi.org/10.1016/j.energy.2012.04.059

Tahir, M., Mulewa, W., Amin, N. A. S., & Zakaria, Z. Y. (2017). Thermodynamic and experimental analysis on ethanol steam reforming for hydrogen production over Ni-modified TiO_2/MMT nanoclay catalyst. *Energy Conversion and Management, 154*, 25-37. doi:https://doi.org/10.1016/j.enconman.2017.10.042

Talebian-Kiakalaieh, A., & Amin, N.A.S. (2016). Theoretical and experimental evaluation of mass transfer limitation in gas phase dehydration of glycerol to acrolein over supported HSiW catalyst. *Journal of the Taiwan Institute of Chemical Engineers, 59*, 11-17. doi:https://doi.org/10.1016/j.jtice.2015.07.011

Thiele, E.W. (1939). Relation between Catalytic Activity and Size of Particle. *Industrial & Engineering Chemistry, 31*(7), 916-920. doi:10.1021/ie50355a027

Venerus, D.C., & Öttinger, H.C. (2018). *A Modern Course in Transport Phenomena* (Illustrated ed.): Cambridge University Press.